2019-01-0966 Published 02 Apr 2019

Detailed Investigation into the Effect of Ozone Addition on Spark Assisted Compression Ignition Engine Performance and Emissions Characteristics

Sayan Biswas and Isaac Ekoto Sandia National Laboratories

Citation: Biswas, S. and Ekoto, I., "Detailed Investigation into the Effect of Ozone Addition on Spark Assisted Compression Ignition Engine Performance and Emissions Characteristics," SAE Technical Paper 2019-01-0966, 2019, doi:10.4271/2019-01-0966.

Abstract

The impact of 50 ppm intake seeding of ozone (O_3) on performance and emissions characteristics was explored in a single-cylinder research engine operated under lean spark assisted compression ignition (SACI) conditions. Optical access into the engine enabled complementary crank angle resolved measurements of in-cylinder O_3 concentration via ultraviolet (UV) light absorption. Experiments were performed at moderate loads (4 - 5 bar indicated mean effective pressure) and low-to-moderate engine speeds (800 - 1400 revolutions per minute). Each operating condition featured a single early main injection and maximum brake torque spark timing. Intake pressure was fixed at 1.0 bar, while intake temperatures were varied between 42 - 80 °C. Moderate amounts of internal residuals (12 - 20%) were retained through the use of positive valve overlap.

Ozone addition was to found stabilize combustion relative to similar conditions without O_3 addition by promoting end gas auto-ignition. Ozone addition was most beneficial for the lowest engine speeds due to the longer available time per cycle for chemically controlled cool flame behavior to occur. Moreover, the homogeneous mixtures and low flame temperatures led to specific NOx emissions of less than 1 g/kg-fuel. From complementary measurements of in-cylinder O_3 decomposition acquired via UV light absorption, rapid decomposition of O_3 into molecular and atomic oxygen coincided with the onset of low-temperature heat release (LTHR). For a given intake temperature and engine speed, the appearance of LTHR was relatively invariant to spark timing and instead was more sensitive to the time at which O_3 decomposition occurred. End gas temperatures at the onset of high-temperature heat release were between 840 and 900 K, which are roughly 200 K cooler than those found in previous studies where intake heating or extensive retained residuals were used to pre-heat the charge. These results demonstrate that O_3 addition increased the charge reactivity of gasoline, and thereby enabled SACI operation for a broader range of conditions.

Introduction

The aggressive move of modern gasoline engines toward challenging lean operating regimes necessitate new and robust combustion strategies such as advanced compression ignition (ACI), where gasoline-like fuels are auto-ignited [1, 2]. In laboratory settings, ACI strategies have achieved high thermal efficiencies with low engine-out emissions of nitrogen oxides (NOx) and particulate matter (PM) through a combination of reduced throttling losses, lower heat transfer, higher compression ratios, and increased charge specific heat ratios. However, the central challenge is to maintain stable and knock-free combustion-defined here as the absence of secondary acoustic pressure oscillations that vibrate engine structures [3]-across the load-speed map.

For full-time ACI, a fuel research octane number (RON) of between 70 and 85 is thought to be optimal [4]. However, widespread adoption of such a low RON gasoline is unlikely since it is unsuitable for conventional spark ignited (SI) combustion due to its poor knock resistance. Instead, low load ACI strategies must tailor the charge reactivity through some combination of intake heating, injection strategy, charge motion, heavy use of retained residuals, and engine geometry [5, 6, 7]. These solutions increase parasitic losses that eat into efficiency gains [8] and add substantial cost/complexity to the engine architecture.

Pure ACI modes are challenging at higher engine loads and speeds due to larger pressure rise rates that lead to increased engine knock. A viable solution is the so-called dual- or mixed-mode strategy where ACI is employed for low loads, with conventional SI used at higher loads [9]. For intermediate loads and speeds, spark assisted compression ignition (SACI) can be used where compression heating from a spark initiated flame kernel leads to end gas auto-ignition [10, 11, 12]. Unthrottled operation and low heat transfer losses preserve the high thermal efficiencies from ACI, while slower pressure rise rates due to significant fuel consumption by the deflagration inhibit engine knock [13, 14]. For spray-guided direct injection (DI) combustion

chambers, a combination of early- and late-cycle injections can stabilize combustion for a wide range of loads by controlling the fuel fraction consumed by the deflagration [12]. However, stratified combustion during the deflagration can lead to significant PM and NOx emissions. Alternatively, exclusive use of early DI is possible provided that end gas temperatures exceed ~1000 K [10, 13, 15, 16]. For moderate compression ratio engines (i.e., below 15:1), extensive charge pre-heat is typically required that can come at the cost of increased heat transfer losses and poor transient response.

Alternatively, ozone (O_3)-a powerful oxidizing chemical agent generated through onboard coronal discharges in intake air-can be used to significantly alter gasoline reactivity, and thereby enable stable auto-ignition with less initial charge heating [17, 18, 19, 20, 21, 22]. During compression, O_3 rapidly decomposes into molecular (O_2) and atomic oxygen (O) at temperatures of around 600 K. For alkanes, the burst of O just before top dead center (TDC) is thought to advance early stage or low-temperature heat release (LTHR) reactions through abstraction of atomic hydrogen (H) from fuel to form hydroxyl (OH) and alkyl radical (R). Hydroxyl likewise abstracts H to make additional R [22, 23]. At high density, low temperature conditions like those present near TDC, R combines with O_2 to form alkyperoxy (RO_2), which then abstracts additional fuel hydrogen to make alkyl hydroperoxide (ROOH). Decomposition of ROOH into alkyloxy radical (RO) and OH then becomes a sustaining source of LTHR radicals [24]. Depending on initial O_3 concentrations, these early LTHR reactions can advance combustion phasing by more than 20 crank angles (CA).

For the present study, the use of intake seeded O_3 was investigated as a way to replace charge pre-heating for stable lean SACI operation with early DI strategies. Experiments were performed in a spray-guided single-cylinder research engine with optical access. Charge concentrations of O_3 were fixed at 50 ppm for all conditions-the peak achievable concentration at the highest 1400 revolution per minute (rpm) engine speed evaluated with the present O_3 generator. Note that O_3 concentration was reduced from 50 to 31 ppm for a single low speed and high intake temperature condition due to excessive knock at the higher concentration. A naturally aspirated intake pressure was maintained for all conditions, with internal residual gas fractions (RGF) of between 12 and 20% achieved through a combination of positive valve overlap (PVO) and moderate exhaust backpressures. Moderate engine loads of between 4 and 5 bar indicated mean effective pressure (IMEP) were examined. Three parameters were separately investigated: 1) Intake temperatures were swept between 42 and 80 °C for a fixed 1000 rpm engine speed; 2) Engine speeds were swept between 800 and 1400 rpm for a fixed 80 °C intake temperature; and 3) A fixed 16.4 mg/cycle fueling rate was maintained for 3 conditions that separately altered either engine speed or intake temperature. Performance and engine-out emissions measurements were complemented by CA resolved O_3 measurements performed via ultraviolet (UV) light absorption and single-zone chemical kinetic modeling of end gas LTHR.

Experimental Setup

Sandia Single-Cylinder Research Engine

All experiments were performed in a 4-valve, single-cylinder, spray-guided, research engine. The combustion chamber features opposed, wall-mounted circular quartz windows (12.7 mm clear aperture) that provide pent roof optical access. Fuel was injected via a centrally mounted Bosch step-hole (HDEV 1.2) injector with 8 uniformly distributed 125 µm diameter nozzles that form a 60° umbrella angle. Combustion was initiated using an NGK long-reach resistor spark plug driven by a 93 mJ Bosch ignition coil. Intake and exhaust cams were set to create 34 CA of PVO centered at TDC. A motoring dynamometer was used to vary engine speeds between 800 and 1400 rpm. A BEI Sensors optical engine encoder with 0.1 CA resolution measured crank angle position. Intake runner and port designs limited swirl and tumble flows to minimize heat transfer losses from in-cylinder generated turbulence. An Aquatherm circulator heat exchanger maintained 90 °C cylinder wall and head temperatures.

Intake air was controlled by a Tescom ER5000 PID (Proportional, Integral, Derivative) pneumatic actuator that precisely regulates the air supply pressures upstream of an orifice plate. Pressures and temperatures were measured in both the intake and exhaust runners, with wire-wrapped resistive heaters and fiberglass insulation in the exhaust runner used to minimize gas temperature changes from heat transfer. A Chromalox circulation heater positioned between the intake plenum and air supply line was used to heat the intake charge up to 80 °C. Cylinder pressure was measured by a Kistler 6125A piezo-electric pressure sensor, with these data used to extract heat release and load data for each cycle.

A two-zone pressure-based heat release analysis was performed where the chamber was separated into burned and unburned zones so that unburned temperatures at the onset of end gas LTHR and HTHR could be estimated. The onset of LTHR was identified from the AHRR profile difference for the same operating conditions with and without O_3 addition. The two-zone model assumed complete combustion in the burned gas region, with the resultant temperature increase estimated from the heat of combustion for the amount of consumed fuel. Heat loss was estimated using the modified Woschni correlation for ACI combustion [25] since most heat release resulted from end gas auto-ignition for all examined conditions here.

Ozone was seeded directly into the intake runner using an Ozone Solutions OZV-4 O_3 generator, with the O_3 concentration set by varying the amount of dry air through the generator using an MKS GE50 mass flow controller. The O_3 concentration out of the generator was directly measured via a Teledyne API 452 O_3 meter. A summary of relevant engine geometry details, valve timings, and operating characteristics is provided in Table 1.

Intake and exhaust pressures were fixed at 1.0 and 1.1 bar respectively, which with the use of PVO produced moderate RGF of between 12 and 20%. To estimate cycle residual gas

TABLE 1 Engine specifications and operating conditions.

Displaced volume [cm^3]	551
Bore/Stroke/Connecting Rod [mm]	86 / 95.1 / 166.7
Geometric Compression Ratio	13:1
Intake Valve Open/Close [CA]†	343 / -145
Exhaust Valve Open/Close [CA]†	160 / -343
Valve Lift [mm]	9.7
Fuel Pressure [bar]	100
Injector Hole Number	8
Injector Cone Angle [°]	60
Injector Orifice Diameter [µm]	125
Intake/Exhaust Pressure [kPa]	100 / 110
Intake Temperature [°C]	42 - 80
Intake O_3 Concentration [ppm]	31 - 50
Engine Speed [rpm]	800, 1000, 1200, 1400
Cycle fueling rates [mg/cycle]	13.4 - 16.9
Charge mass equivalence ratio	0.37 - 0.45
RGF [%]	12 - 20
SOI [CA]†	-330

† 0 CA corresponds to TDC of the compression stroke

mass, the pressure at intake valve closure (IVC) was divided into partial pressures for intake air, fuel, and residual gas. Each partial pressure was then expressed in terms of the mixture specific gas constant, temperature, mass, and IVC cylinder volume using the ideal gas law. Note that the measured exhaust temperature was used for the residual gas temperature. After rearranging, the residual gas mass was estimated as follows:

$$m_r = \frac{R_{exh}T_{exh}}{P_{IVC}V_{IVC}} + \frac{m_{\text{int}}R_{\text{int}}T_{\text{int}} + m_f R_f T_f}{R_{exh}T_{exh}} \quad (1)$$

Subscripts *r*, *int* , *exh* and *f*, denote residual, intake, exhaust, and fuel respectively. The known residual gas composition from exhaust emissions measurements along with the estimate of residual mass from equation 1 was then used to determine IVC composition. Temperature at IVC was then solved from the ideal gas equation using the pressure and volume at IVC, total cylinder mass, and a gas constant determined from the new estimate for IVC composition. Because no external EGR was used, lean charge equivalence ratios (ϕ) of below 0.6 were maintained for all conditions examined here.

Research-grade RD587 gasoline with a RON of 92.1 and an octane sensitivity of 7.3 was used for all tests. Important fuel properties are summarized in Table 2.

TABLE 2 RD587 gasoline fuel properties.

Liquid Density @ 15 °C [g/L]	748
LHV [MJ/kg]	41.87
H/C ratio	1.972
O/C ratio	0.033
Research Octane Number	92.1
Octane Sensitivity	7.3
T10 / T50 / T90 [°C]	57 / 98 / 156

Pollutant emissions were sampled from the exhaust plenum using heated sampling lines to minimize water and fuel condensation. Dry emissions of carbon monoxide (CO), carbon dioxide (CO_2), and O_2 were measured via a CAI 600 NDIR/Oxygen Multi-Component analyzer. Hydrocarbon (HC) emissions were measured by a CAI 600 HFID. Measurements of CO and HC were used in conjunction with measured fuel injection and air flow rates to calculate combustion efficiency. Nitrogen oxide emissions were measured using a CAI 600 HCLD NO/NOx chemiluminescence analyzer. Although PM was not measured, these emissions were expected to be very low due to the combination of early DI and lean ϕ. A schematic of the engine setup is provided in Figure 1.

For each experiment, the engine was motored for around 30 seconds with the O_3 generator turned on so that uniform and steady O_3 concentrations accumulated in the intake runner. The engine was then fired for around 90 seconds using a predefined spark timing (ST) and early DI with a start of injection (SOI) set at -330 CA. After the 90 second warm-up period, the injection quantity and ST were gradually adjusted to the desired experiment set point. Once combustion and emissions measurements stabilized, a single 100 cycle set of data was collected for each operating point. The engine was then motored, with the whole process repeated for the next experiment.

Ozone Absorption

Bulk-averaged in-cylinder O_3 concentrations were measured on a crank angle basis using UV light absorption, as illustrated in Figure 2. Broadband continuous wave light from a Spectra-Physics 250 Watt Xenon arc lamp was partially collimated by a condensing lens and then passed through the combustion chamber via two Nd:YAG 4th harmonic laser line mirrors that selectively reflected only the 266 nm UV light from the lamp. The O_3 absorption cross-section for 266 nm light (σ_{O3}) is 0.937×10^{-17} cm^2/molecule [26]. A third laser line mirror

FIGURE 1 Schematic of the optical engine, gas supply system, O_3 generator, and emissions measurement setup.

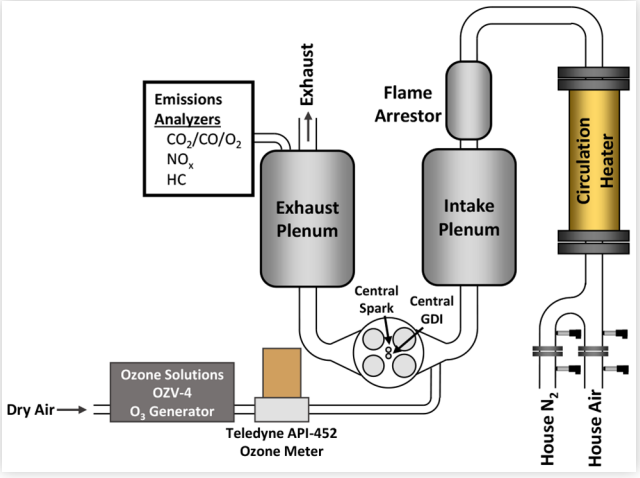

FIGURE 2 Schematic representation of the O_3 absorption diagnostic.

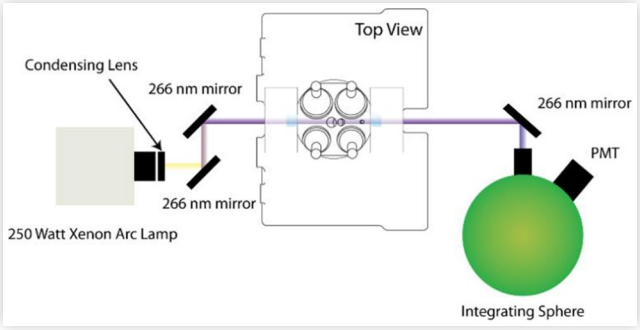

directed the 266 nm lamp light into an integrating sphere, where the light was detected by a Pacific Instruments 3150RF photomultiplier tube (PMT). The setup minimized the effects of beam steering due to thermal gradients within the combustion chamber.

The in-cylinder O_3 concentration, X_{O3}, was quantified using 3 independent datasets that each consisted of 100 ensemble-averaged full-cycle measurements. The "background" dataset was acquired with the lamp light blocked to account for ambient light. The "reference" dataset, I_{ref}, was acquired with the lamp light unblocked and the desired engine fueling schedule performed minus the seeded O_3 to account for light absorption from the ambient gas and any light attenuation from the optical setup. Finally, the "target" dataset, I, was identical to I_{ref} but with O_3 seeding. Only data from the closed portion of the cycle were considered.

Crank angle resolved X_{O3} was calculated from the O_3 partial pressure, p_{O3}, with p_{O3} computed from the Beer-Lambert Law as follows:

$$X_{O_3} = \frac{p_{O_3}}{p} = \ln\left(\frac{I_{ref}}{I}\right)\frac{k_B T}{pB\sigma_{O_3}} \tag{2}$$

Here, k_B is the Boltzmann constant (1.381×10^{-23} [$J \cdot K^{-1}$]) and B is the bore diameter and T is the unburned gas temperature from the heat release analysis was used. The specific heat ratio was calculated from the known composition at IVC and updated with the calculated temperature from the previous step.

Note that for fueled conditions, added O_3 can stabilize combustion for the target cycles while misfiring for the associated reference cycles. As a result, high amounts of hot residual CO_2 that absorbs UV light at elevated temperatures [27] are present in the target cycle, but not the reference cycle. Moreover, hydroperoxyl (HO_2) and hydrogen peroxide (H_2O_2) are prominent combustion intermediates during LTHR and HTHR reactions that likewise absorb UV light [22, 28, 29]. Accordingly, target cycle absorption not from O_3 can differ relative to the reference condition. To combat this effect, the spark plug was not discharged so that combustion was suppressed for both the reference and target cycles. Additionally, intake temperatures were increased such that the range of IVC temperatures achieved matched those from the corresponding fired cycles.

Single-Zone Chemical Model

To evaluate chemical kinetic pathways responsible for associated fuel oxidation by generated O, Chemkin-Pro 0D homogeneous reactor simulations were performed [30]. The simulation was initialized with the estimated experiment IVC composition and was constrained to the measured pressure and unburned gas temperature through main compression so that processes relevant to O_3 decomposition, radical formation, and fuel oxidation could be evaluated. The Lawrence Livermore National Laboratory detailed gasoline surrogate mechanism [31] appended with O_3 oxidation chemistry from Masurier et al. [17] was used, which produced a combined mechanism comprised of 2028 species and 8636 reactions. The gasoline was modeled as a 5-component gasoline surrogate (46.6% iso-octane, 17.8% n-heptane, 9.9% ethanol, 6.0% 1-hexene, and 19.7% toluene by liquid volume) that matched the broad molecular composition and reactivity characteristics of RD587 gasoline [7].

Engine Results

Ozone concentration at IVC was fixed at 50 ppm except for a single condition where it was dropped to 31 ppm to minimize knock. Note that engine combustion was completely unstable without the added O_3 for all examined conditions. The first subsection describes results for a sweep of intake temperature (42 - 80 °C) with a fixed 1000 rpm engine speed. For each condition, the fueling rate at maximum brake torque (MBT) ST was adjusted until the minimum achievable load was met, provided that the coefficient of variation (CoV) of IMEP was below 3%, the ringing intensity (RI) was below 1 MW/m^2, and NOx emissions were below 1 g/kg-fuel. In the second subsection, results for engine speed sweeps (800 - 1400 rpm) with a fixed 80 °C intake temperature are discussed. Once again, the fueling rate was set to reach the minimum achievable load provided that the same criteria described above were met. Finally, in the third subsection results are presented for conditions with a fixed 16.5 mg/cyc fueling rate at the baseline 1000 rpm engine speed and 80 °C intake temperature, with either the engine speed (1400 rpm) or intake temperature (42 °C) varied. These results are complemented by single-zone Chemkin-Pro simulation results that are used to evaluate the impact of O_3 addition on end gas LTHR.

Intake Temperature Sweep

Values of IMEP, 50% mass fraction burn angle (CA50), and CoV of IMEP are plotted for each intake temperature condition as a function of ST in Figure 3. The ST and CA50 values are provided in crank angle degrees after top dead center (°aTDC). The minimum achievable load decreased from 5.0 bar IMEP for an intake temperature of 42 °C to 4.3 bar IMEP when the intake temperature was increased to 80 °C due to increased end gas reactivity that enabled auto-ignition for leaner mixtures. While MBT ST retarded with higher intake

FIGURE 3 Plots of IMEP, CA50, and CoV of IMEP as a function of ST for a sweep of intake temperatures (42 - 80 °C) and a fixed 1000 rpm engine speed.

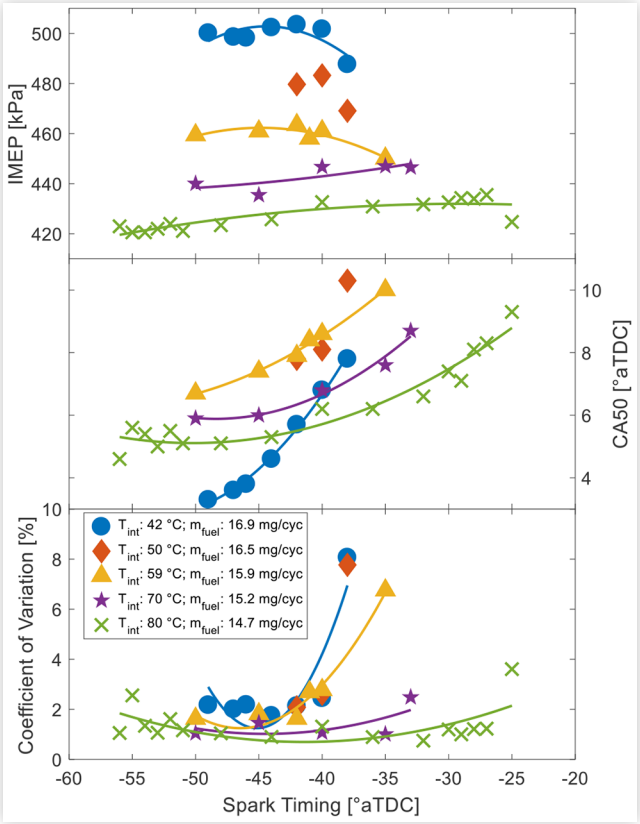

temperatures, IMEP values were within 1% of the MBT values for a broad range of ST.

Major cycle characteristics for each condition in the intake temperature sweep are summarized in Table 3. Note that the charge mass equivalence ratio (ϕ') is used here instead of the conventional definition of ϕ because it provides a representative comparison of total charge dilution by retained residuals and excess-air relative to stoichiometric conditions [32]. It is defined as follows:

$$\phi' \equiv \frac{m_f / m_{main}}{m_f / m_{air\ stoich}} \quad (3)$$

Here m is mass, and the subscripts refer to the injected fuel (f), main charge ($main$), and stoichiometric air ($air\ stoic$) mass values.

From Table 3 it is evident that RGF values decreased with higher intake temperatures (and hence lower fueling rates). As a result, the IVC charge temperature was relatively invariant across the sweep as lower intake temperatures were partially offset by higher fractions of retained residual heat.

For all intake temperatures, a retard in ST led to an associated retard in CA50. The effect was most pronounced for the lowest intake temperature (42 °C), highest load condition (5.0 bar IMEP). As intake temperatures increased and load decreased, the profile slope became increasingly shallow. The result suggests that for higher intake temperature, end gas

TABLE 3 Values of fueling rate, ϕ', IVC temperature, and RGF for a sweep of intake temperatures (42 - 80 °C) and a fixed 1000 rpm engine speed.

Intake Temperature [°C]	42	50	59	70	80
Fueling Rate [mg/cycle]	16.9	16.5	15.9	15.2	14.7
ϕ'	0.43	0.42	0.41	0.41	0.40
IVC Temperature [K]	365	358	369	385	380
RGF [%]	19.2	16.9	17.0	17.4	15.8

auto-ignition was less dependent on the initial deflagration. For most intake temperatures, MBT CA50 was around 8° aTDC. The exception was for the lowest intake temperature condition, where optimal CA50 was closer to 5° aTDC. For further CA50 retard, combustion became highly unstable.

Profiles of cylinder pressure and apparent heat release rate (AHRR) at MBT conditions are plotted in Figure 4 for each intake temperature. All profiles feature evidence of LTHR reactions that start around -20° aTDC, with HTHR that starts very close to TDC. Little evidence of deflagration related heat release prior to the LTHR period was observed for profiles despite ST that were generally much earlier.

For conditions with intake temperatures between 50 and 80 °C, HTHR phasing was closely matched. Of these profiles, the condition with the highest intake temperature (and thus lowest load) had the highest peak AHRR value. Peak AHRR decreased as the intake temperature was lowered (and thus load increased), with the decline more than offset by higher AHRR values between the LTHR and HTHR periods. It is unclear if this heat release is evidence of the deflagration, or the result of

FIGURE 4 Cylinder pressure and AHRR profiles for a sweep of intake temperatures (42 - 80 °C), MBT spark timing, and a fixed 1000 rpm engine speed.

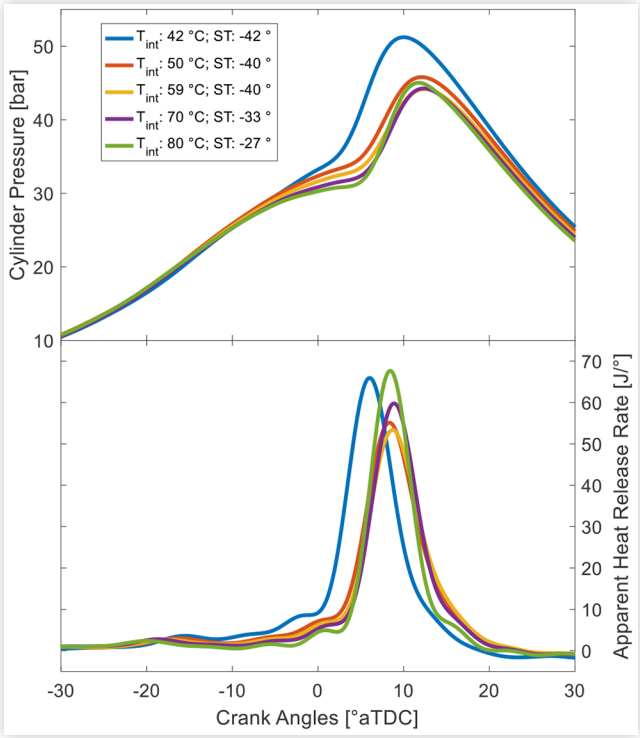

intermediate-temperature heat release (ITHR) [33]. For the lowest intake temperature condition, HTHR phasing was advanced by around 3 CA relative to the other profiles.

Values of LTHR and HTHR onset are plotted in Figure 5 for all conditions as a function of CA50 to more closely examine the associated relationship. Firstly, it is evident that LTHR phasing was heavily dependent on intake temperature, with a roughly 5.5 CA difference between the lowest and highest intake temperature conditions for a given CA50 value. Furthermore, for a fixed intake temperature, a retard in LTHR led to a more significant retard in CA50. Conversely, HTHR onset and CA50 collapsed onto a single positive linear correlation for all conditions, which is unsurprising given that most cycle heat release occurred during the relatively short HTHR period.

An important metric for auto-ignition transition is the unburned end gas temperature at the onset of LTHR and HTHR reactions. Respective values are plotted in Figure 6 as a function of the LTHR onset time for a given condition. For LTHR reactions, these values varied between 705 and 740 K for most conditions. For changes in intake temperature, the unburned end gas temperature at LTHR was inversely proportional to LTHR onset due to the modestly lower IVC temperatures for conditions with lower intake temperatures (Table 3). Unburned end gas temperatures at HTHR varied between 840 and 900 K for most conditions and were likewise inversely proportional to LTHR onset. These end gas temperatures are about 200 K lower than comparable reported values for SACI operation where extensive amounts of negative valve overlap was used to retain residual heat [13, 16].

FIGURE 5 Phasing of LTHR and HTHR onset as a function of CA50 for a sweep of intake temperatures (42 - 80 °C) and a fixed 1000 rpm engine speed.

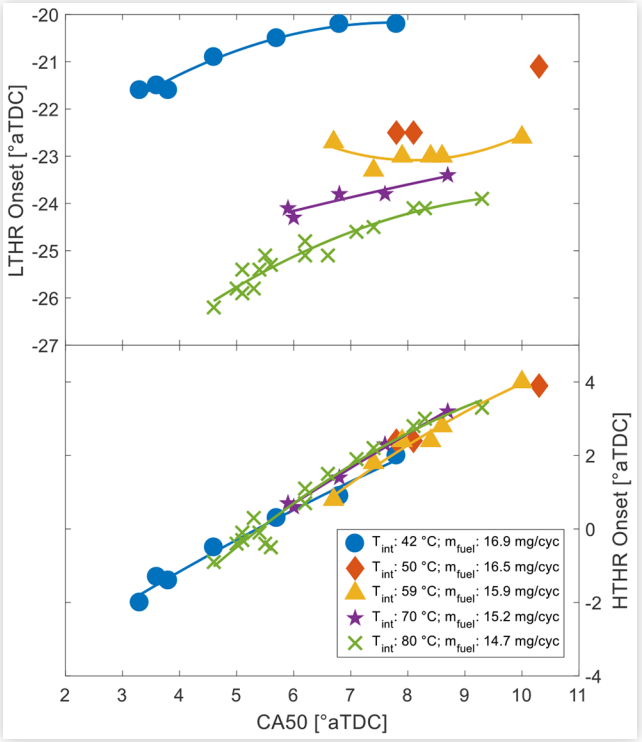

FIGURE 6 Comparison of the unburned gas temperatures at LTHR and HTHR onset as a function of LTHR onset time for a sweep of intake temperatures (42 - 80 °C) and a fixed 1000 rpm engine speed.

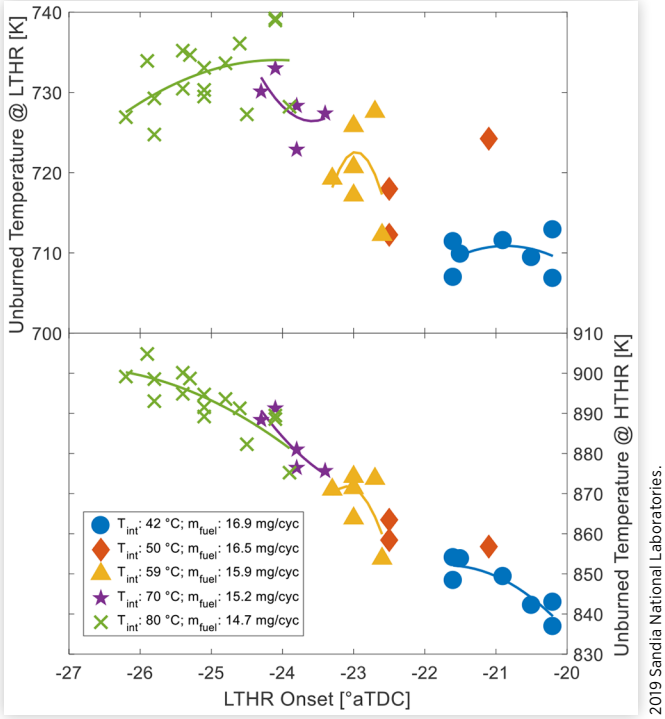

To examine the impact of O_3 decomposition on auto-ignition kinetics, measured O_3 profiles with IVC temperatures of 361 and 384 K are plotted in Figure 7 alongside AHRR profiles from Figure 4 that zoom in on the LTHR period. As discussed in the experimental methods section, the range of IVC temperatures for the O_3 measurements was matched to the fired experiment values (Table 3). Ozone profiles are plotted on a semi-log scale to more clearly highlight when rapid thermal decomposition into O and O_2 occurs. Note that there was increased absorbance starting around -25° aTDC that was not present in the reference datasets. As stated in the introduction, this increased absorbance was likely from HO_2 formed during LTHR reactions. Although the spurious absorbance was not desired, it nonetheless is a convenient marker of LTHR onset.

For both profiles, rapid O_3 thermal decomposition started around -40 aTDC, and was nearly complete by -20 aTDC. Thermal O_3 decomposition for the higher IVC temperature condition (384 K) concluded just before the appearance of LTHR for the fired conditions with the highest intake temperature (i.e., 70 and 80 °C). All three conditions had closely matched IVC temperatures. Moreover, the increased absorbance just after decomposition closely correlated with the LTHR period for these fired conditions. Similarly, thermal O_3 decomposition for the lower IVC temperature condition (361 K) preceded the appearance of LTHR for fired conditions with the lowest intake temperatures (i.e., 42 and 50 °C). The subsequent increase in absorbance once again strongly correlated with the fired condition LTHR periods. These results strongly

FIGURE 7 Measured in-cylinder O_3 concentration for a low (361 K) and high (384 K) IVC temperature condition that spanned the range of IVC temperatures for the fired experiments. A close-in view of the corresponding LTHR period for the profiles from Figure 4 is included for comparison.

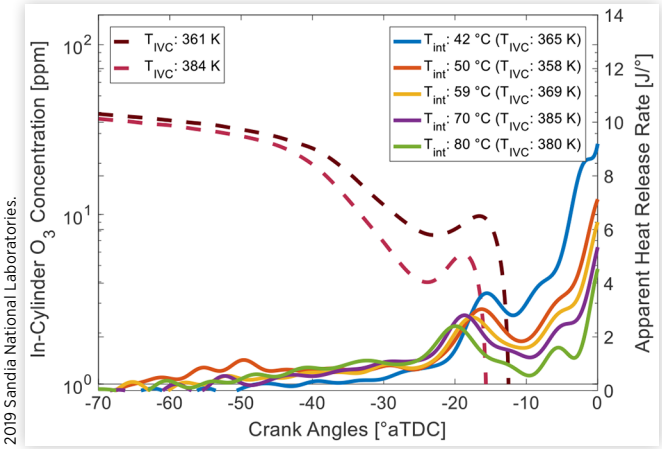

suggest that LTHR onset was most sensitive to the timing of O_3 thermal decomposition, and less so on ST.

Measurements of ITE and combustion efficiency are plotted in Figure 8 as a function of CA50. Peak ITE values between 38 and 39% were achieved for all conditions, which demonstrates that the strategy can produce large regions of high efficiency, even for the low-to-moderate loads examined here. Moreover, good peak combustion efficiencies of around 95% were achieved for each intake temperature condition.

FIGURE 8 Comparison of ITE combustion efficiency as a function of CA50 for an intake temperatures sweep (42 - 80 °C) with fixed 1000 rpm engine speed.

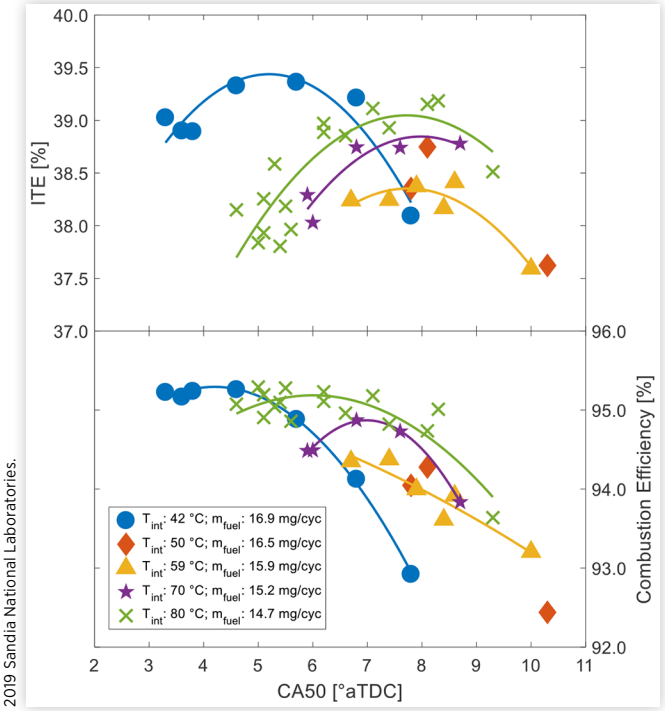

When combustion phasing was overly retarded, the drop in ITE was mostly due to decreased combustion efficiency that resulted from less stable combustion.

Finally, specific NOx emissions and RI values are plotted in Figure 9 as a function of the estimated peak burned gas temperature since both variables are expected to strongly correlate with this parameter. For all conditions, relatively low peak burned gas temperatures of between 1790 and 1880 K kept specific NOx emissions below 1 g/kg-fuel. As expected, NOx emissions had a modest inverse dependence on peak burned gas temperature, with most points collapsing to a single linear correlation. The exception was the lowest intake temperature condition (42 °C), which had a much stronger dependence on peak burned gas temperatures. Values for RI were likewise proportional to peak burned gas temperatures, although the collapse was less consistent.

Engine Speed Sweep

The present subsection describes results for sweeps of engine speed (800, 1000, 1200, and 1400 rpm) with a fixed 80 °C intake temperature. Table 4 summarizes major parameters for each condition. Note that data from the 1000 rpm condition is reproduced from the first subsection and is included here for reference.

As with the intake temperature sweeps, the fueling rate and ST were adjusted iteratively until a minimum load was achieved provided that CoV of IMEP was below 3%, NOx emissions were below 1 g-kg/fuel, and RI was below 1 MW/m^2. The lowest minimum fueling rate occurred for an engine

FIGURE 9 Comparison of NOx and RI plotted as a function of peak burned gas temperature for an intake temperatures sweep (42 - 80 °C) with fixed 1000 rpm engine speed.

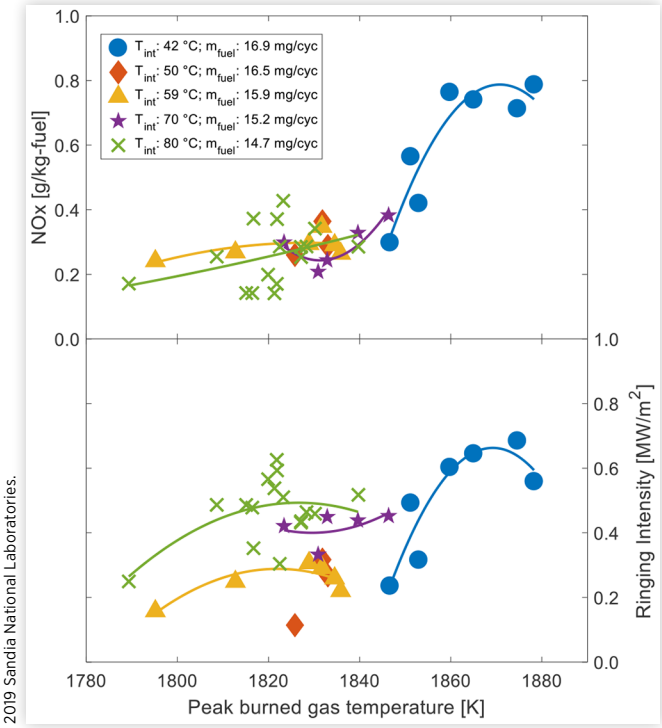

TABLE 4 Values of fueling rate, ϕ', IVC temperature, and RGF for a sweep of engine speeds (800 - 1400 rpm) and fixed 80 °C intake temperature.

Engine Speed [rpm]	800	1000	1200	1400
Fueling Rate [mg/cycle]	13.6	14.7	15.6	16.5
ϕ'	0.37	0.40	0.42	0.45
IVC Temperature [K]	383	380	389	383
RGF [%]	18.6	15.8	15.9	12.5

speed of 800 rpm and steadily increased by around 1 mg/cycle for each 200 rpm increase in engine speed. Peak RGF values occurred for the lowest 800 rpm engine speed condition (18.6%) due to better volumetric efficiency during PVO, and steadily decreased to around 12.5% for the highest 1400 rpm engine speed. Bulk temperatures at IVC were closely matched, as the lower residual fractions were offset by higher residual temperatures for the higher engine speed conditions.

Similar to the previous subsection, values of IMEP, CA50, and CoV of IMEP are plotted for each engine speed as a function of ST in Figure 10. The minimum achievable load ranged from 3.8 bar IMEP for the lowest 800 rpm engine speed to 4.9 bar IMEP when engine speed was increased to 1400 rpm. Note that for the slowest 800 rpm condition, sustained auto-ignition was possible after the first cycle without further assistance from the spark, as intake charge heating from retained residuals alone was sufficient to promote auto-ignition. As a result, performance and emissions metrics were completely unaffected by ST. Accordingly, only 2 data points are plotted here. Conversely, for the higher 1200 and 1400 rpm conditions, there was a very narrow range of ST (-55 to -52 CA) where stable combustion was possible. For the highest engine speed 1400 rpm condition in particular, CA50 was very sensitive to ST.

FIGURE 10 Comparison of IMEP, CA50, and CoV of IMEP as a function of ST for a sweep of engine speeds (800 - 1400 rpm) and fixed 80 °C intake temperature.

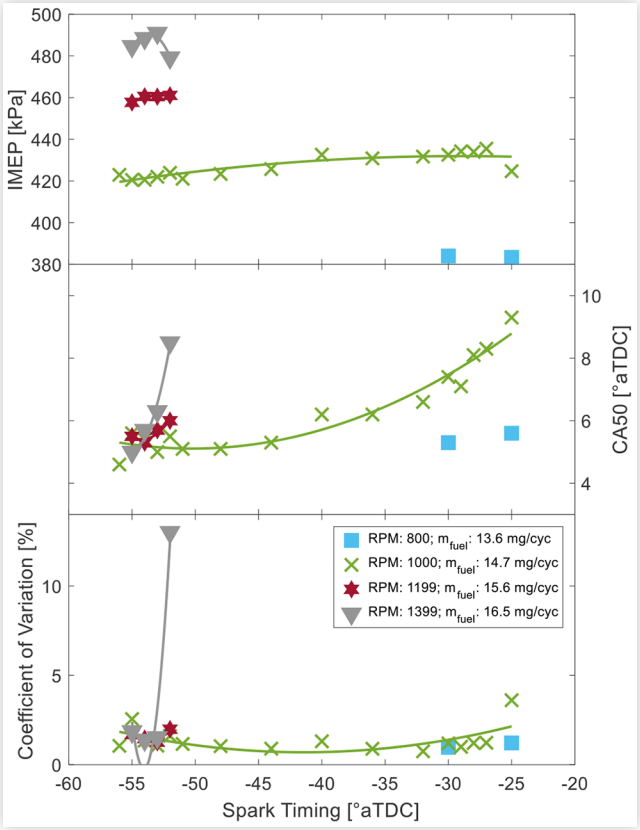

Profiles of AHRR for MBT conditions at each engine speed are plotted in Figure 11. For each profile, clear evidence of LTHR was once again observed. Moreover, LTHR onset was consistent at around -25 CA, and the total amount of LTHR was also well-matched. For the two lowest speed conditions (800 and 1000 rpm) there was no evidence of heat release between the LTHR and HTHR periods. The only major difference between these profiles was a roughly 3 CA advance in HTHR for the 800 rpm condition. For the higher engine speed conditions, there was substantial heat release between the LTHR and HTHR periods. Again, it is unclear if this heat release was due to a weak deflagration initiated by the spark, or was the result of ITHR reactions. Like the lower speed conditions, the profiles for the higher speed conditions had very similar features.

Complementary measurements of in-cylinder O_3 concentration for the range of engine speeds from the fired experiments are plotted in Figure 12 along with a close-up view of LTHR period heat release rates for the fired conditions. Once again, late-cycle absorbance from LTHR reactions was observed for the O_3 measurements. In-cylinder O_3 concentrations gradually declined early in the cycle before the onset of rapid O_3 decomposition, which started around -45 CA for all engine speeds. Note that the only major difference for the different engine speeds was that O_3 decomposition generally advanced with lower engine speeds. This was likely due to the longer residence times that enabled a greater amount of decomposition during the cooler early portion of the cycle. Rapid thermal O_3 decomposition concluded by around -25 CA, which is around the time of LTHR onset for all fired conditions.

FIGURE 11 AHRR profiles for a sweep of engine speeds (800 - 1400 rpm), MBT ST, and fixed 80 °C intake temperature.

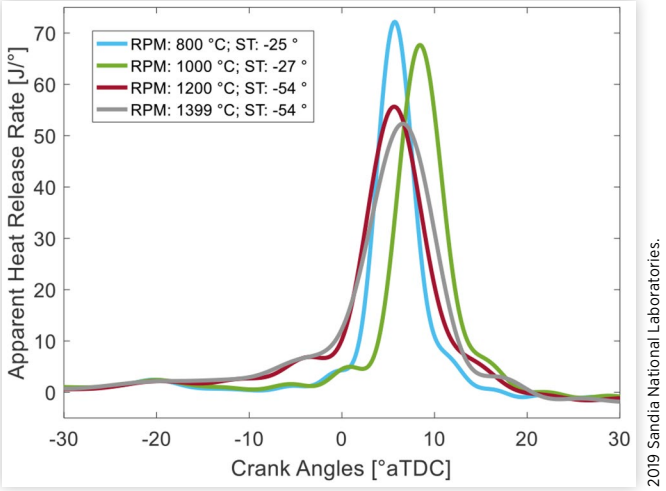

FIGURE 12 Measured in-cylinder O_3 concentration and a close-up view of LTHR period heat release rates for an engine speed sweep (800 - 1400 rpm).

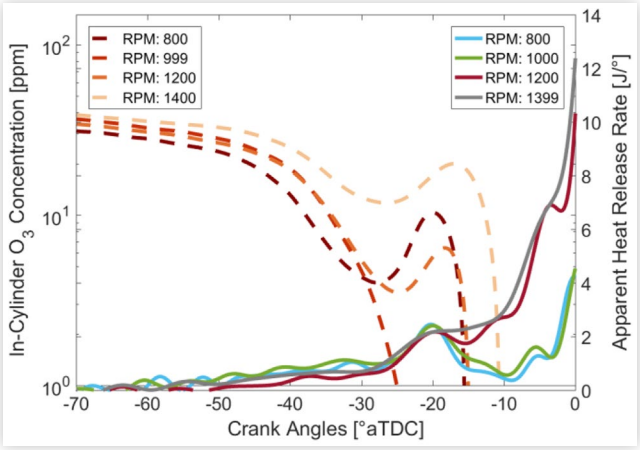

Values of LTHR and HTHR onset along with ITE and combustion efficiency are plotted in Figure 13 as a function of CA50. For engine speeds at or below 1200 rpm, LTHR onset values were relatively invariant to CA50. The highest 1400 rpm engine speed condition, however, had a much broader range of LTHR onset values that were positively correlated with CA50 despite a relatively narrow range of ST. Values for HTHR onset once again had a positive linear correlation with CA50 for all engine speeds.

Peak ITE values exceeded 39% for most conditions except for the lowest speed 800 rpm condition where ITE was 37.2%. Peak combustion efficiency was also above 94% for all engine speeds. For the highest engine speed condition, the drop in combustion efficiency with CA50 retard was the principal driver for the sharp drop in ITE.

Finally, specific NOx emissions and RI as a function of peak burned gas temperature are plotted in Figure 14. The range of peak burned gas temperatures was similar to the intake temperature sweep conditions from the previous subsection (1760 - 1940 K). Specific NOx emissions once again had a positive linear correlation with peak burned gas temperature. Values for RI had a negative linear correlation with engine speed (and hence load), but a positive correlation for fixed speed and fueling rate.

Fixed Fueling Rate

The final subsection discusses the impact of engine speed and intake temperature variations for 3 operating conditions with a common 16.5 mg/cycle fueling rate. The "Baseline" condition featured a lower engine speed (1000 rpm) and the highest intake temperature examined in the present study (81 °C). A "Low Heating" condition was selected to investigate how the Baseline condition changes with lower intake temperature (50 °C). The final "Moderate Speed" condition with a 1400 rpm engine speed was used to examine how the Baseline condition results were affected by shorter combustion residence times. Only results with MBT ST are presented here. Note that the Baseline condition end gas was too reactive for any ST, which

FIGURE 13 Comparison of LTHR/HTHR timing, ITE, and combustion efficiency as a function of CA50 over a sweep of engine speeds (800 - 1400 rpm) for a fixed 80 °C intake temperature.

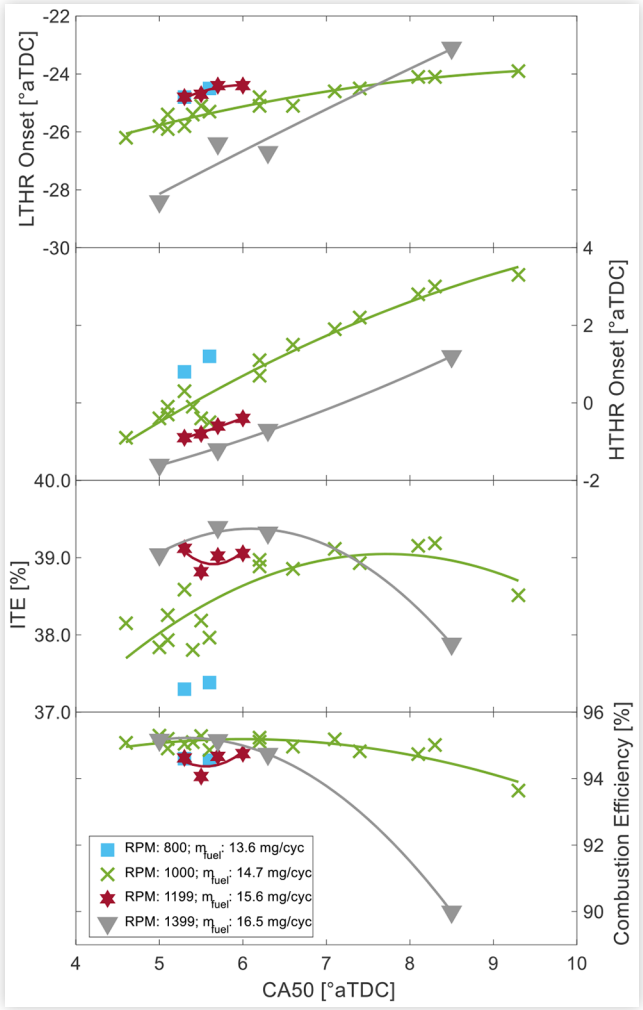

led to substantial engine knock. Accordingly, the O_3 concentration was dropped from 50 to 31 ppm to reduce the end gas reactivity.

Major characteristics for each condition are summarized in Table 5. Optimal ST significantly advanced from the Baseline to the Low Heating condition (-28 to -40 aTDC), and advanced even further for the Moderate Speed condition (-54 aTDC). The Low Heating condition had an IVC temperature that was roughly 25 K cooler than the other two conditions. It also had the highest RGF at 16.9%.

Profiles of AHRR for each condition are plotted in Figure 15. The highest peak AHRR values were achieved for the Baseline condition (1000 rpm, 81 °C T_{int}). Note that while intake O_3 was lowered to avoid knock, the condition was still borderline knocking and thus experienced more intense HTHR. Peak AHRR values were of similar magnitude for the Low Heating (1000 rpm, 50 °C T_{int}) and Moderate Speed (1400 rpm, 80 °C T_{int}) conditions, although HTHR phasing was roughly 3 CA earlier for the Moderate Speed condition. The Moderate Speed condition also exhibited the largest amount

FIGURE 14 The effect of engine speeds ranging from 800 to 1400 rpm on ITE, NOx, efficiency, and ringing intensity as a function of CA50 for a fixed intake temperature, 80 °C.

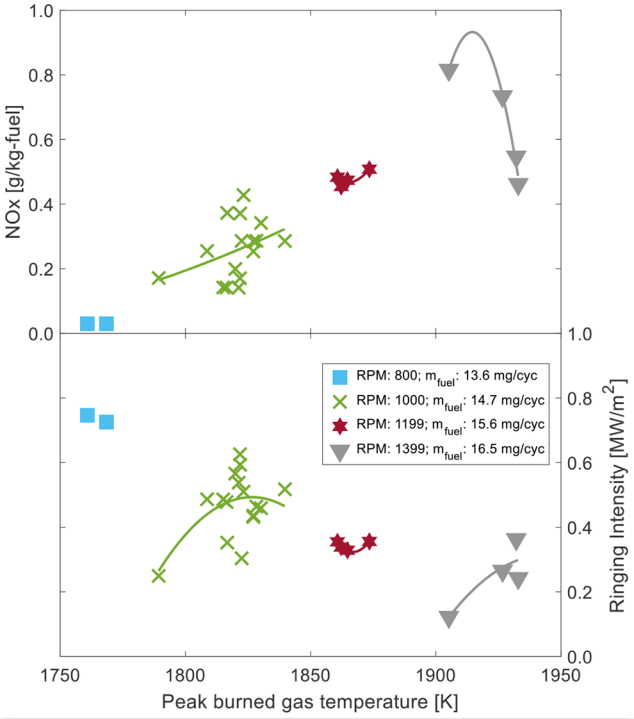

TABLE 5 Values of engine speed, intake temperature, IMEP, ST, IVC temperature, and RGF for the Baseline, Low Heating, and Moderate Speed conditions. Fueling rates were fixed at 16.5 mg/cycle.

Condition	Baseline	Low Heating	Moderate Speed
Engine Speed [rpm]	1000	1000	1400
Intake Temperature [°C]	81	50	80
Intake O_3 concentration [ppm]	31	50	54
IMEP [kPa]	469	483	491
Spark Timing [°aTDC]	-28	-40	-54
IVC Temperature [K]	386	358	383
RGF [%]	15.4	16.9	12.5

of heat release between the LTHR and HTHR periods. For the Low Heating condition, these values were far less intense, while there was none observed for the Baseline condition.

The onset timing of LTHR and HTHR reactions for each condition is plotted in Figure 16. It is notable that LTHR onset had a strong positive linear correlation with CA50. However, no firm conclusions can be made given that there are only 3 points. The Moderate Speed (1400 rpm, 80 °C T_{int}) condition had the earliest LTHR onset, likely due to the combination of elevated IVC temperature that advanced the rate of O_3 decomposition and the early ST that gave more time for the deflagration to develop. Despite having similar intake temperatures, LTHR onset for the Baseline condition (1000 rpm, 81 °C T_{int})

FIGURE 15 Profiles of AHHR profiles for the Baseline (1000 rpm, 81 °C T_{int}), Low Heating (1000 rpm, 50 °C T_{int}), and Moderate Speed (1400 rpm, 80 °C T_{int}) conditions. Fueling rates were fixed at 16.5 mg/cycle.

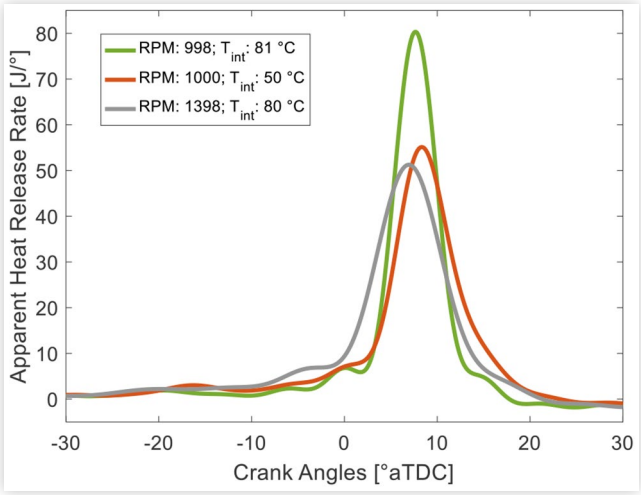

FIGURE 16 The timing of LTHR and HTHR onset as a function of CA50 for the Baseline (1000 rpm, 81 °C T_{int}), Low Heating (1000 rpm, 50 °C T_{int}), and Moderate Speed (1400 rpm, 80 °C T_{int}) conditions. Fueling rates were fixed at 16.5 mg/cycle.

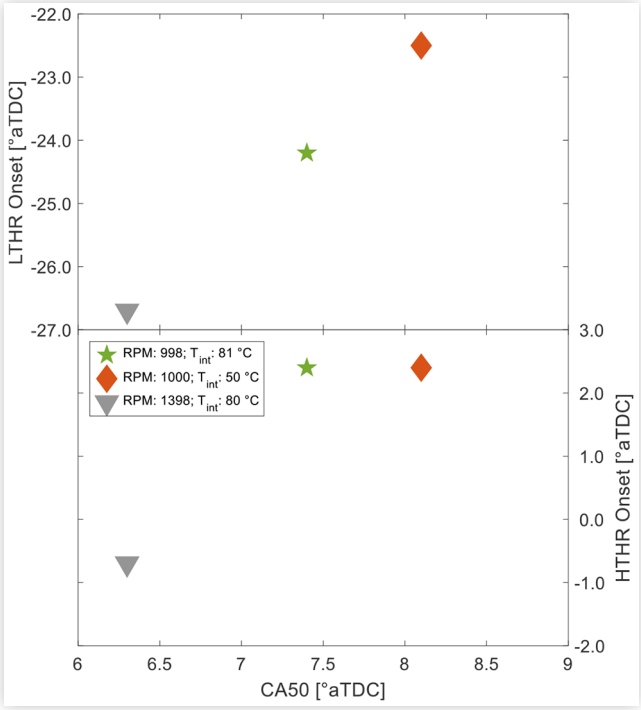

was retarded by around 3 CA. In part, this was due to the fact that lower O_3 concentrations were previously found to delay LTHR onset [22]. Despite the fact that the Low Heating condition (1000 rpm, 50 °C T_{int}) had the most retarded LTHR onset, the small amount of heat release between the LTHR and HTHR periods was enough to accelerate HTHR onset to a value that was comparable to the Baseline value. Because much

of the fuel energy had been consumed by this point, peak HTHR values were lower.

Plots of ITE in Figure 17 illustrate that the Moderate Speed condition had the highest overall efficiency of 39.3%. The Low Heating condition ITE was somewhat lower at 38.7%, mostly due to a slight decrease in both combustion efficiency and combustion stability. It is interesting to note that the Baseline condition had by far the lowest ITE value at 37.7%, despite having the highest combustion efficiency and lowest CoV of IMEP relative to the other 2 conditions. The only plausible explanation is an increase in heat transfer losses that resulted from the higher peak combustion temperatures and possible wall layer separation due to weak knocking behavior.

Plots of specific NOx emission in Figure 18 continue to exhibit a positive linear dependence with peak burned gas temperature, although the correlation with ringing intensity is less clear. RI values between 0.2 and 0.3 MW/m^2 were achieved for the Moderate Speed and Low Heating conditions despite having vastly different peak burned temperatures (1830 vs. 1930 K). The Baseline condition, however, had an RI value that was more than double despite a peak burned gas temperature (1940 K) that was only marginally higher than the Moderate Speed value. However, RI also depends on the peak value of the temporal pressure gradient, which was highest for the Baseline condition.

FIGURE 17 Comparison of ITE, and combustion efficiency, and CoV of IMEP as a function of CA50 for the Baseline (1000 rpm, 81 °C T_{int}), Low Heating (1000 rpm, 50 °C T_{int}), and Moderate Speed (1400 rpm, 80 °C T_{int}) conditions. Fueling rates were fixed at 16.5 mg/cycle.

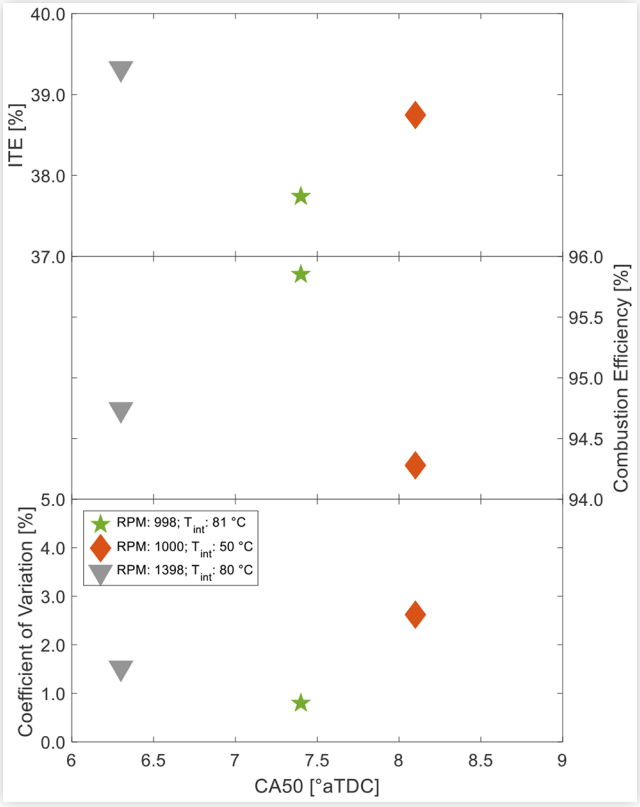

2019 Sandia National Laboratories.

FIGURE 18 ITE, NOx, efficiency, and ringing intensity for the Baseline (1000 rpm, 81 °C T_{in}), Low Heating (1000 rpm, 50 °C T_{in}), and Moderate Speed (1400 rpm, 80 °C T_{in}) conditions. Fueling rates were fixed at 16.5 mg/cycle.

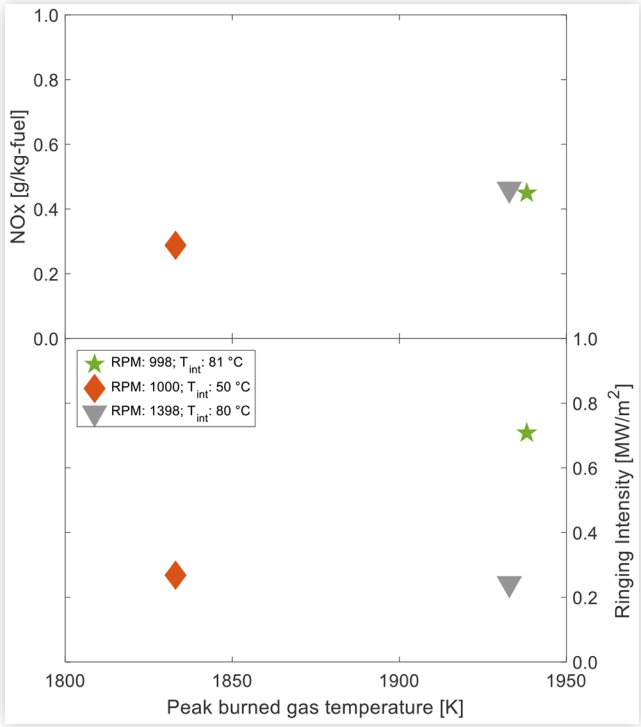

LTHR Kinetic Pathway Analysis

To understand the major chemical drivers for improved autoignition chemistry with O_3 addition, 0D kinetic simulations with detailed gasoline chemistry were performed. The simulations are initialized at IVC and continue through the main compression so that all processes relevant to O_3 decomposition, radical formation, and fuel oxidation can be evaluated. A schematic of dominant LTHR reaction pathways described in the Introduction is illustrated in Figure 19 that highlights how generated O leads to multiple sustaining production pathways for R and OH. Note that an additional pathway where RO_2 undergoes internal isomerization to form hydroperoxyalkyl radical (QOOH) is included for completeness.

Simulations were performed with and without O_3 addition, with all other boundary conditions fixed to evaluate the importance of the reaction pathways from Figure 19 on LTHR chemistry. Profiles of AHRR from the Moderate Speed (1400 rpm, 80 °C T_{int}) condition are plotted in Figure 20 along with the corresponding simulation results with and without O_3 addition. Note that similar results were observed for the other two conditions, and thus are excluded here for brevity. Onset of LTHR from the simulation results with O_3 addition closely match the corresponding experiment results. Conversely, no evidence of LTHR was observed for the simulations without O_3 addition.

Predicted O_3 concentrations are relatively stable early in the cycle, and start a rapid decline beginning around -40

FIGURE 19 Schematic of LTHR reaction pathways initialized by O formed from thermal decomposition of O_3. Red and blue arrows highlight the sustained source of R and OH radicals respectively.

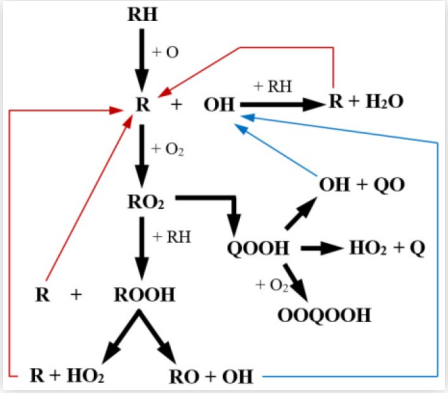

FIGURE 20 Measured AHRR profile from the Moderate Speed (1400 rpm, 80 °C T_{in}) condition along with complementary AHRR profiles from the 0D Chemkin simulations with (solid) and without (dashed) O_3 addition (top). These values are compared to cycle predictions of O_3 and important fuel oxidation radicals (middle), along with model-predicted fuel ROC values for the dominant LTHR pathways highlighted in Figure 19 (bottom).

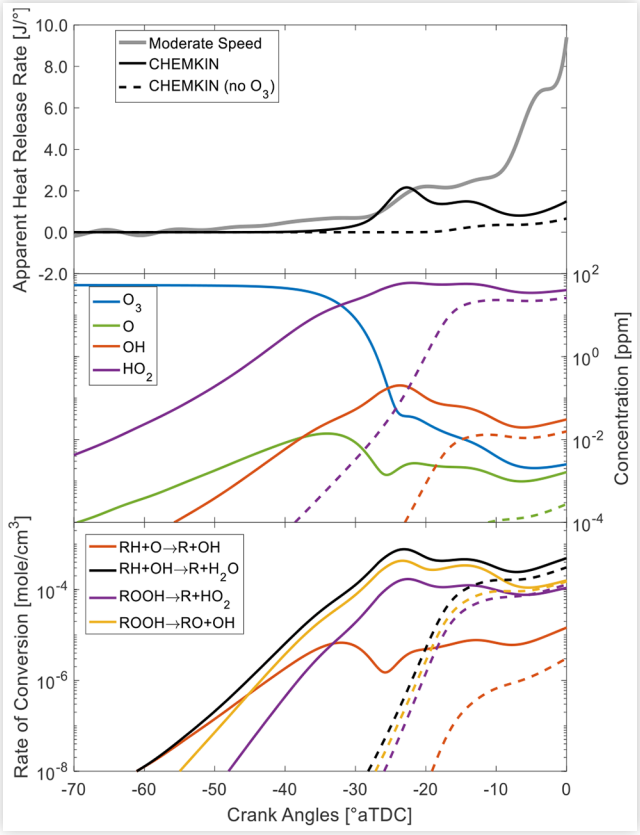

aTDC with negligible concentrations by -25 aTDC. These results agree well with the corresponding experimental results from Figure 12. Predicted concentrations of O never exceed 0.01 ppm due to its rapid consumption by fuel molecules. Nonetheless, accelerated O_3 decomposition leads to much earlier formation of O, OH, and HO_2.

The final plot of Figure 20 is of profiles for the rate of conversion (ROC) for the major reaction pathways from Figure 19. Note that the ROC values represent the summation of all possible reactions, and not just a specific hydrocarbon. Moreover, the R used here does not exclusively refer to alkyl radicals, but instead represents all hydrocarbon radicals. As expected, the presence of O leads to early formation of R and OH, with the resultant OH quickly abstracting more fuel H to make R and water. Conversion rates for H abstraction by O are relatively modest throughout since the supply of O is limited by the rate of O_3 thermal decomposition. Accordingly, H abstraction by OH quickly dominates R formation since OH formation is augmented by subsequent unimolecular decomposition of ROOH.

Conclusions

In the present study, performance and emissions characteristics were evaluated for lean SACI operation with 50 ppm of the oxidizing agent, O_3 that was seeded into the intake charge. Experiments were performed in an optically accessible single-cylinder research engine with a spray-guided design and 13:1 compression ratio. For all experiments, intake pressure was fixed at 1.0 bar, with no external EGR used. A combination of intake back-pressure and modest PVO was used to produce a moderate amount of retained residuals that was used to slightly heat the subsequent charge. Sweeps of intake temperature (42 - 80 °C) and engine speed (800 - 1400 rpm) were performed. For each condition in the respective sweeps, the single early DI fueling rate was adjusted until the minimum achievable load was met provided that the CoV of IMEP was below 3%, the RI was below 1 MW/m², and NOx emissions were below 1 g/kg-fuel. As a result, modest engine loads (3.8 to 5.0 bar IMEP) and lean values of ϕ' (0.37 - 0.45) were produced. Performance and emissions results were augmented by quantitative measurements of CA resolved in-cylinder O_3 concentration obtained using a UV absorption diagnostic. Experimental measurements of AHRR and in-cylinder O_3 are complemented by single-zone Chemkin-Pro simulation results that are used to evaluate O_3 decomposition and associated LTHR chemical pathways. Major findings are as follows:

- For a fixed 1000 rpm engine speed, the minimum achievable load decreased with increased charge temperature due to increased end gas reactivity that enabled auto-ignition for leaner mixtures. For all intake temperatures, a retard in ST led to an associated retard in CA50. IMEP values were within 1% of the MBT values for a broad range of ST.
- Peak ITE values between 38 and 39% were achieved for most conditions, which demonstrates that the strategy can produce high efficiencies for moderate loads.

- Ozone addition stabilized combustion relative to similar conditions without O_3 by increasing end gas reactivity. Estimated end gas temperatures at HTHR onset were up to 200 K lower than what was achieved for previous studies.
- Ozone addition was most beneficial for the lowest engine speeds due to longer cycle residences times for chemically controlled heat release to occur.
- For all conditions examined here, optimal LTHR onset was between -20° and -30° aTDC with HTHR onset near TDC. Both values correlated positively with CA50.
- Rapid decomposition of O_3 into O_2 and O preceded LTHR onset, which indicates LTHR onset was more sensitive to O_3 decomposition than to ST.
- As engine speeds increased or charge temperatures cooled, end gas auto-ignition was much more dependent on the spark induced deflagration due to the slower kinetic rates and shorter residence times.
- A kinetic analysis of O_3 addition reveals that alkyl radical formation is quickly dominated by OH abstraction of fuel H due to sustained OH formation by subsequent ROOH unimolecular decomposition.

The present results demonstrate that O_3 addition can expand the range of applicability for SACI operation without the use of substantial intake heating or stratified combustion that results in poor emissions performance. Nonetheless, further investigation is needed to explore O_3 decomposition behavior, particularly in the presence of EGR constituents. Moreover, in-cylinder chemiluminescence imaging is needed to clarify if the observed intermediate heat release between is the results of auto-ignition chemistry or is the results of a spark-induced deflagration.

References

1. Dec, J.E., "Advanced Compression-Ignition Engines-Understanding the In-Cylinder Processes," *P. Combust. Inst.* 32(2):2727-2742, 2009, doi:10.1016/j.proci.2008.08.008.
2. Saxena, S. and Bedoya, I.D., "Fundamental Phenomena Affecting Low Temperature Combustion and HCCI Engines, High Load Limits and Strategies for Extending These Limits," *Prog Energ Combust* 39(5):457-488, 2013, doi:10.1016/j.pecs.2013.05.002.
3. Dernotte, J., Dec, J.E., and Ji, C., "Investigation of the Sources of Combustion Noise in HCCI Engines," *SAE Int. J. Engines* 7(2):730-761, 2014, doi:10.4271/2014-01-1272.
4. Kalghatgi, G.T., "Developments in Internal Combustion Engines and Implications for Combustion Science and Future Transport Fuels," *P. Combust. Inst.* 35(1):101-115, 2015, doi:10.1016/j.proci.2014.10.002.
5. Steeper, R.R. and Davisson, M.L., "Analysis of Gasoline Negative-Valve-Overlap Fueling via Dump Sampling," *SAE Int. J. Engines* 7(2):762-771, 2014, doi:10.4271/2014-01-1273.
6. Kolodziej, C., Kodavasal, J., Ciatti, S., Som, S. et al., "Achieving Stable Engine Operation of Gasoline Compression Ignition Using 87 AKI Gasoline Down to Idle," SAE Technical Paper 2015-01-0832, 2015, doi:10.4271/2015-01-0832.
7. Wolk, B., Ekoto, I., and Northrop, W., "Investigation of Fuel Effects in Negative Valve Overlap Reforming Chemistry Using Gas Chromatography," *SAE Int. J. Engines* 9(2), 2016, doi:10.4271/2016-01-0753.
8. Ekoto, I., Wolk, B., and Northrop, W., "Energy Analysis of Low-Load Low-Temperature Gasoline Combustion with Auxiliary-Fueled Negative Valve Overlap," *SAE Int. J. Engines* 10(3):1238-1255, 2017, doi:10.4271/2017-01-0729.
9. Lawler, B.J. and Filipi, Z.S., "Integration of a Dual-Mode SI-HCCI Engine Into Various Vehicle Architectures," *J Eng Gas Turb Power* 135(5):2013.
10. Lavoie, G.A., Martz, J., Wooldridge, M., and Assanis, D., "A Multi-Mode Combustion Diagram for Spark Assisted Compression Ignition," *Combustion and Flame* 157(6):1106-1110, 2010, doi:10.1016/j.combustflame.2010.02.009.
11. Persson, H., Hultqvist, A., Johansson, B., and Remón, A., "Investigation of the Early Flame Development in Spark Assisted HCCI Combustion Using High Speed Chemiluminescence Imaging," SAE Technical Paper 2007-01-0212, 2007, doi:10.4271/2007-01-0212.
12. Reuss, D.L., Kuo, T.-W., Silvas, G., Natarajan, V., and Sick, V., "Experimental Metrics for Identifying Origins of Combustion Variability During Spark-Assisted Compression Ignition," *Int. J. Engine Res.* 9(5):409-434, 2008, doi:10.1243/14680874JER01108.
13. Olesky, L.M., Martz, J.B., Lavoie, G.A., Vavra, J. et al., "The Effects of Spark Timing, Unburned Gas Temperature, and Negative Valve Overlap on the Rates of Stoichiometric Spark Assisted Compression Ignition Combustion," *Appl Energ* 105:407-417, 2013, doi:10.1016/j.apenergy.2013.01.038.
14. Middleton, R.J., Olesky, L.K.M., Lavoie, G.A., Wooldridge, M.S. et al., "The effect of spark timing and negative valve overlap on Spark Assisted Compression Ignition combustion heat release rate," *P. Combust. Inst.* 35(3):3117-3124, 2015, doi:10.1016/j.proci.2014.08.021.
15. Olesky, L.K.M., Middleton, R.J., Lavoie, G.A., Wooldridge, M.S., and Martz, J.B., "On the Sensitivity of Low Temperature Combustion to Spark Assist Near Flame Limit Conditions," *Fuel* 158:11-22, 2015, doi:10.1016/j.fuel.2015.05.012.
16. Olesky, L.M., Lavoie, G.A., Assanis, D.N., Wooldridge, M.S., and Martz, J.B., "The Effects of Diluent Composition on the Rates of HCCI and Spark Assisted Compression Ignition Combustion," *Appl Energ* 124:186-198, 2014, doi:10.1016/j.apenergy.2014.03.015.
17. Masurier, J.B., Foucher, F., Dayma, G., and Dagaut, P., "Homogeneous Charge Compression Ignition Combustion of Primary Reference Fuels Influenced by Ozone Addition," *Energ Fuel* 27(9):5495-5505, 2013, doi:10.1021/ef401009x.
18. Masurier, J.B., Foucher, F., Dayma, G., and Dagaut, P., "Ozone Applied to the Homogeneous Charge Compression Ignition Engine to Control Alcohol Fuels Combustion," *Appl Energ* 160(Supplement C):566-580, 2015, doi:10.1016/j.apenergy.2015.08.004.
19. Masurier, J.-B., Foucher, F., Dayma, G., and Dagaut, P., "Investigation of Iso-Octane Combustion in a Homogeneous

Charge Compression Ignition Engine Seeded by Ozone, Nitric Oxide and Nitrogen Dioxide," *P. Combust. Inst.* 35(3):3125-3132, 2015, doi:10.1016/j.proci.2014.05.060.

20. Truedsson, I., Rousselle, C., and Foucher, F., "Ozone Seeding Effect on the Ignition Event in HCCI Combustion of Gasoline-Ethanol Blends," SAE Technical Paper 2017-01-0727, 2017, doi:10.4271/2017-01-0727.
21. Pinazzi, P.M. and Foucher, F., "Potential of Ozone to Enable Low Load Operations of a Gasoline Compression Ignition (GCI) Engine," SAE Technical Paper 2017-01-0746, 2017, doi:10.4271/2017-01-0746.
22. Ekoto, I. and Foucher, F., "Mechanisms of Enhanced Reactivity with Ozone Addition for Advanced Compression Ignition," SAE Technical Paper 2018-01-1249, 2018, doi:10.4271/2018-01-1249.
23. Smekhov, G.D., Ibraguimova, L.B., Karkach, S.P., Skrebkov, O.V., and Shatalov, O.P., "Numerical Simulation of Ignition of a Hydrogen-Oxygen Mixture in View of Electronically Excited Components," *High Temp* 45(3):395-407, 2007.
24. Zádor, J., Taatjes, C.A., and Fernandes, R.X., "Kinetics of Elementary Reactions in Low-Temperature Autoignition Chemistry," *Prog Energ Combust* 37(4):371-421, 2011, doi:10.1016/j.pecs.2010.06.006.
25. Chang, J., Güralp, O., Filipi, Z., Assanis, D. et al., "New Heat Transfer Correlation for an HCCI Engine Derived from Measurements of Instantaneous Surface Heat Flux," SAE Technical Paper 2004-01-2996, 2004, doi:10.4271/2004-01-2996.
26. Gorshelev, V., Serdyuchenko, A., Weber, M., Chehade, W., and Burrows, J.P., "High Spectral Resolution Ozone Absorption Cross-Sections - Part 1: Measurements, Data Analysis and Comparison with Previous Measurements around 293 K," *Atmos Meas Tech* 7(2):609-624, 2014, doi:10.5194/amt-7-609-2014.
27. Schulz, C., Koch, J.D., Davidson, D.F., Jeffries, J.B., and Hanson, R.K., "Ultraviolet Absorption Spectra of Shock-Heated Carbon Dioxide and Water between 900 and 3050 K," *Chem Phys Lett* 355(1-2):82-88, 2002, doi:10.1016/S0009-2614(02)00190-2.
28. Kijewski, H. and Troe, J., "Study of the Pyrolysis of H2O2 in the Presence of H2and CO by Use of UV Absorption of HO2," *Int J Chem Kinet* 3(3):223-235, 1971, doi:10.1002/kin.550030304.
29. Molina, L.T. and Molina, M.J., "UV Absorption Cross-Sections of HO2NO2 Vapor," *J Photochem* 15(2):97-108, 1981.
30. Ansys, CHEMKIN-PRO, 2017, http://www.ansys.com/products/fluids/ansys-Chemkin-pro.
31. Mehl, M., Pitz, W.J., Westbrook, C.K., and Curran, H.J., "Kinetic Modeling of Gasoline Surrogate Components and Mixtures under Engine Conditions," *P. Combust. Inst.* 33:193-200, 2011, doi:10.1016/j.proci.2010.05.027.
32. Kodavasal, J., Lavoie, G.A., Assanis, D.N., and Martz, J.B., "The Effect of Diluent Composition on Homogeneous Charge Compression Ignition Auto-Ignition and Combustion Duration," *P. Combust. Inst.* 35:3019-3026, 2015, doi:10.1016/j.proci.2014.06.152.
33. Mehl, M., Pitz, W., Sarathy, M., Yang, Y., and Dec, J.E., "Detailed Kinetic Modeling of Conventional Gasoline at Highly Boosted Conditions and the Associated Intermediate Temperature Heat Release," SAE Technical Paper 2012-01-1109, 2012, doi:10.4271/2012-01-1109.

Contact Information

Isaac Wesley Ekoto
Sandia National Laboratories
P.O. Box 969, MS 9053
Livermore, CA 94551, USA
iekoto@sandia.gov

Acknowledgments

The authors would like to thank Alberto Garcia, Gary Hubbard, and Keith Penney for their dedicated support of the Gasoline Combustion Fundamentals Laboratory. We moreover would like to thank Marco Mehl with his assistance developing the 5-component gasoline surrogate. The work was performed at the Combustion Research Facility, Sandia National Laboratories, Livermore, CA. Financial support was provided by the U.S. Department of Energy, Vehicle Technologies Office. Sandia National Laboratories is a multi-mission laboratory managed and operated by National Technology and Engineering Solutions of Sandia, LLC., a wholly owned subsidiary of Honeywell International, Inc., for the U.S. Department of Energy's National Nuclear Security Administration under contract DE-NA0003525.

Definitions/Abbreviations

ϕ - Equivalence ratio
ϕ' - Charge mass equivalence ratio
σ_{O_3} - Ozone absorption cross-section
ACI - Advanced compression ignition
AHRR - Apparent heat release rate
aTDC - After top dead center
B - Bore diameter [m]
CA - Crank angle referenced to main TDC [°]
CA50 - 50% cumulative burn angle
CO - Carbon monoxide
CO_2 - Carbon dioxide
CoV - Coefficient of variation
DI - Direct injection
EGR - Exhaust gas recirculation
EVC/EVO - Exhaust valve close/open
DI - Direct injection
H - Atomic hydrogen
HC - Hydrocarbon
H/C - Hydrogen-to-carbon ratio
H_2O - Water
HO_2 - Hydroperoxyl
H_2O_2 - Hydrogen peroxide
HC - Hydrocarbon
HTHR - High-temperature heat release
I_{ref} - Reference intensity

IMEP - Indicated mean effective pressure
ITE - Indicated thermal efficiency
ITHR - Intermediate-temperature heat release
IVC/IVO - Intake valve close/open
k_B - Boltzmann constant [J/K]
LHV - Lower heating value [kJ/g]
LTHR - Low-temperature heat release
m - Mass [kg]
MBT - Maximum brake torque
N_2 - Nitrogen
NO - Nitric oxide
NOx - Nitrogen oxide
NVO - Negative valve overlap
O - Atomic oxygen
O_2 - Molecular oxygen
O_3 - Ozone
OH - Hydroxyl
p,P - Pressure [Pa]
PID - Proportional, Integral, Derivative
PM - Particulate matter
PMT - Photomultiplier tube
ppm - Parts per million
PVO - Positive valve overlap
R - Alkyl radical,
R - Specific gas constant [J/kg-K]
RGF - Residual gas fraction
RI - Ringing intensity [Mw/m^2]
RO - Alkyloxy radical
RO_2 - Alkylperoxy
ROC - Rate of consumption [mole/cm^3]
ROOH - Alkyl hydroperoxide
RON - Research octane number
rpm - Revolutions per minute
SACI - Spark assisted compression ignition
SI - Spark ignition
SOI - Start of fuel injection
ST - Spark timing
T - Temperature [K]
T10/T50/T90 - 10%, 50%, and 90% boiling points
TDC - Top dead center
V - Volume
UV - Ultraviolet

Subscripts

air - Air
exh - Exhaust
f - Fuel
int - Intake
main - Main intake charge
r - Residual
stoich - Stoichiometric condition

ISSN 0148-7191